

Inelastic light scattering in the spin cluster Mott insulator Cu_2OSeO_3

R. B. Versteeg,^{1,*} C. Boguschewski,¹ P. Becker,² and P. H. M. van Loosdrecht^{1,†}

¹*Institute of Physics 2, Faculty of Mathematics and Natural Sciences,
University of Cologne, Zùlpicher StraÙe 77, D-50937 Cologne, Germany*

²*Institute of Geology and Mineralogy, Faculty of Mathematics and Natural
Sciences, University of Cologne, Zùlpicher StraÙe 49b, D-50674 Cologne, Germany*

(Dated: May 24, 2022)

Clusters of single spins form the relevant spin entities in the formation of long-range magnetic order in spin cluster Mott insulators. Such type of spin order bears resemblance to molecular crystals, and we therefore may expect a prototypical spin wave spectrum which can be divided into low-energy external and high-energy internal cluster spin wave modes. Here, we study high-energy spin cluster excitations in the spin cluster Mott insulator Cu_2OSeO_3 by means of spontaneous Raman scattering. Multiple high-energy optical magnon modes are observed, of which the Raman-activity is shown to originate in the Elliot-Loudon scattering mechanism. Upon crossing the long-range ordering transition temperature the magnetic modes significantly broaden, corresponding to scattering from localized spin excitations within the spin clusters. Different optical phonon modes show a strong temperature dependence, evidencing a strong magnetoelectric coupling between optical phonons and the high-energy spin cluster excitations. Our results support the picture that Cu_2OSeO_3 can be regarded as a solid-state molecular crystal of spin nature.

I. INTRODUCTION

Strong electron-electron correlations lie at the origin of the formation of a vast range of exotic charge, orbital, and spin states in solids.^{1,2} For the majority of quantum materials, the single ionic site spin, orbitals, and charge form the entities for the description of the ordering and resulting collective excitations. However, in a peculiar subclass of quantum materials, known as cluster Mott-insulators,^{3,4} the single site description does not hold, and instead “molecules” (or clusters) of spin, orbital, and charge degree of freedom form the relevant entities to describe the emerging physical phenomena. This solid-state molecule formation has, for instance, been found to underlie the nature and speed limit of the Verwey-transition in magnetite,^{5,6} and allowed to demonstrate Young-interference in the resonant inelastic x-ray scattering process from iridate dimer molecules.⁷

The solid-state molecule formation may be fluctuating, as in the case of dimer formation in the resonating valence bond condensed state,^{8,9} but we can also identify “rigid” molecular crystals of charge, orbital and spin degree of freedom. The latter situation occurs in materials with a disproportionation in structural bond lengths,⁸ with a resulting subdivision of strong and weak electronic interactions. This situation leads to a collective excitation spectrum which can be subdivided into low-energy *external* and high-energy *internal* modes, in close resemblance to the vibrational spectrum of the true molecular crystal.^{10,11} An understanding of the collective excitation spectrum below and above the “crystallization” temperature is important as it provides the dynamic fingerprint of the solid-state molecular crystal nature of cluster Mott insulators.

In this context, we investigate the temperature dependent inelastic light scattering response of the spin cluster Mott insulator Cu_2OSeO_3 . While this material

was initially of high interest because of the skyrmion metamagnetism,^{12–14} a second surprise came with the insight that effective $S=1$ Cu_4 spin clusters form the relevant spin entities for the formation of long-range order, instead of the single site Cu^{2+} $S=\frac{1}{2}$ spins.^{15,16} This picture was consecutively firmly established with electron spin resonance and inelastic neutron scattering studies deep inside the ordered phase, which showed that Cu_2OSeO_3 has a characteristic spin wave spectrum comprising of low-energy cluster-external and high-energy cluster-internal modes.^{17–19} The spin cluster excitation nature in the paramagnetic phase has only been minimally discussed.^{20,21} A multitude of the high-energy spin cluster excitations have been observed in different Raman studies,^{21–23} and used in a time-resolved Raman study to track photoinduced spin cluster disordering,²¹ but insight in the underlying magnetic light scattering mechanism is still incomplete. We address these issues in greater detail in this article.

With spontaneous Raman-spectroscopy we observed multiple high-energy spin excitations in Cu_2OSeO_3 , which can be assigned to different spin cluster transitions. Their Raman-activity can be traced back to the Elliot-Loudon scattering mechanism. While the spin cluster excitations correspond to well-defined optical magnons in the long-range ordered phase, they cross over into localized cluster-internal spin excitations above T_C , resulting in a broad magnetic scattering continuum. Different optical phonon modes show a strong temperature dependence, evidencing a strong magnetoelectric coupling between optical phonons and the high-energy spin cluster excitations. Our results support the picture that Cu_2OSeO_3 can be regarded as a solid-state molecular crystal of spin nature.

II. SPIN CLUSTER FORMATION

Before turning to the Raman spectroscopy results, we summarize the most important conclusions from the works Refs. 15–19, which discuss the spin cluster order and excitations in Cu_2OSeO_3 in considerable detail. This summary will be beneficial in order to assign the Raman-active cluster modes and deduce the inelastic light scattering mechanism. Figure 1a shows the magnetic unit cell of Cu_2OSeO_3 . The localized Cu^{2+} $S=1/2$ spins reside on the vertices of corned-shared tetrahedra in a distorted pyrochlore lattice.¹⁵ DFT+ U calculations reveal that these tetrahedra can be separated into tetrahedra of “stronger” and “weaker” exchange energy scales.^{15,17} A few exchange couplings are indicated in Fig. 1a as $J_{F,s}$, $J_{AF,s}$, $J_{F,w}$, and $J_{AF,w}$, where the subscripts refer to (anti)ferromagnetic (AF/F) and strong or weak exchange (s/w). An additional antiferromagnetic exchange $J_{AF,OO}$ couples spins across a hexagon of alternating Cu-I and Cu-II sites (not shown).²⁴ The inversion symmetry between spin is absent both inside the cluster and in between clusters.²⁵ This results in a nonzero Dzyaloshinskii-Moriya-interaction D across all drawn paths, with a D/J -ratio on the order of 0.1 – 0.6 for different Cu^{2+} - Cu^{2+} bonds.^{15,26}

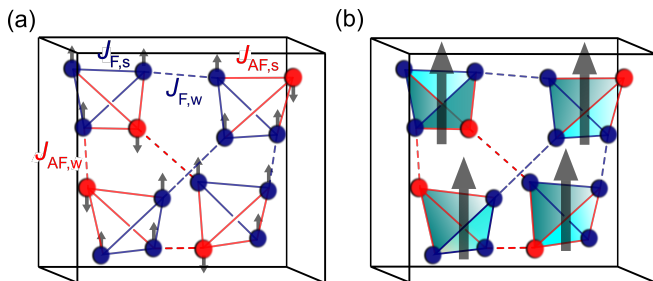


Figure 1. (a) The magnetic unit cell of Cu_2OSeO_3 . A few exchange interactions are indicated as $J_{F,s}$, $J_{AF,s}$, $J_{F,w}$, and $J_{AF,w}$ where the subscripts refer to (anti)ferromagnetic (AF/F) and strong or weak exchange (s/w). The blue lines are predominantly ferromagnetic exchange couplings and the red lines predominantly antiferromagnetic exchange couplings. The full lines are strong exchange couplings and the dashed lines weak exchange couplings. Not shown is the antiferromagnetic exchange path $J_{AF,OO}$ which couples spins across a hexagon of alternating Cu-I and Cu-II sites. (b) The strong exchange interaction leads to effective $S=1$ spin clusters.

The strong Heisenberg (and Dzyaloshinskii-Moriya exchange) interactions couple four localized $S=1/2$ spins into a three-up-one-down $S=1$ entity. Here the Cu-II ions couple ferromagnetically through $J_{F,s}$, while the Cu-I ion couples antiferromagnetically to the Cu-II ions through $J_{AF,s}$. The Cu_4 cluster formation occurs far above the long-range ordering temperature of $T_C \approx 58$ K, as evidenced from the temperature dependence of the inverse magnetic susceptibility, which in the paramagnetic phase shows gradual crossover between a $S=1/2$

Curie-constant at high temperatures and a $S=1$ Curie-constant at lower temperatures.¹⁹ The Curie-constant crossover is characteristic of materials with strong and weak exchange interactions.²⁷

For a single isolated cluster the relevant exchange paths are the strong paths $J_{F,s}$ and $J_{AF,s}$. The spin Hamiltonian for the isolated cluster is thus given by:

$$\hat{\mathcal{H}}_0 = J_{AF,s} \hat{S}_1 \cdot (\hat{S}_2 + \hat{S}_3 + \hat{S}_4) + J_{FM,s} (\hat{S}_2 \cdot \hat{S}_3 + \hat{S}_3 \cdot \hat{S}_4 + \hat{S}_4 \cdot \hat{S}_2) \quad (1)$$

Here \hat{S}_1 is the spin angular momentum operator for the spin on the Cu-I ion, and \hat{S}_2 , \hat{S}_3 , and \hat{S}_4 for the Cu-II ions. The eigenstates are notated as $|S, S^z\rangle_R$. Here S indicates the total spin quantum number of the cluster. The secondary spin quantum number (the spin momentum projection along the z-axis) is indicated by S^z . The symmetry label R refers to the irreducible representations of the single cluster’s C_{3v} point group (this is the cluster symmetry when only the magnetic Cu^{2+} ions are considered). Under the symmetry C_{3v} the $2^4 = 16$ -dimensional Hilbert space of a single tetrahedron splits into the ground state A_1 -triplet $|1, S^z\rangle_{A_1}$, and two E_1 and E_2 singlets, one A_1 quintet $|2, S^z\rangle_{A_1}$, and two E_1 and E_2 triplets excited states $|1, S^z\rangle_{E_1/E_2}$.¹⁶ The corresponding (isolated) spin cluster wave functions are indicated in Table I, and will be later of use when discussing the Raman-activity of the cluster excitations. From the form of the wave functions it becomes apparent that the cluster wave functions are highly entangled.

The interaction between clusters is to first approximation captured by the tetrahedral mean field (TMF) Hamiltonian:

$$\hat{\mathcal{H}}_{\text{TMF}} = \hat{\mathcal{H}}_0 + \hat{\mathcal{H}}' [\langle \hat{S}_1 \rangle, \langle \hat{S}_{2,3,4} \rangle, J_{FM,w}, J_{AF,w}, J_{AF,OO}] \quad (2)$$

The perturbation term $\hat{\mathcal{H}}'$ depends on the mean magnetic fields exerted by the Cu-I ions and Cu-II ions, which are proportional to the magnetic moments $\langle \hat{S}_1 \rangle$, and $\langle \hat{S}_{2,3,4} \rangle$ respectively, the weak inter-cluster exchange couplings $J_{FM,w}$ and $J_{AF,w}$, and a hexagonal antiferromagnetic weak exchange path $J_{AF,OO}$.²⁴ A further refinement to the model was done in the second quantization formalism.¹⁶ The resulting energies of the cluster states at the Γ -point with corresponding degeneracies are indicated in table 2.

As a result of the inter-cluster interactions the excited state quintet furthermore mixes into the ground state of the isolated cluster model:

$$|g_{\text{TMF}}\rangle = \cos \frac{\alpha}{2} |1, 1\rangle_{A_1} + \sin \frac{\alpha}{2} |2, 1\rangle_{A_1} \quad (3)$$

Here $S^z = +1$ has been chosen as the ground state. Note that in the interacting model the total spin quantum number S isn’t a good quantum number anymore.

The factor $\frac{\alpha}{2}$ gives the amount of quintet mixing, for which $\alpha \approx 0.58$ was found.¹⁶ A possible perturbation of the excited state wave functions by the inter-tetrahedral interaction is not discussed in the aforementioned papers. In the later discussion of the Raman spectra we therefore use the perturbed ground state $|g_{\text{TMF}}\rangle$ instead of $|1\rangle$, but use the unperturbed single cluster wave functions $|2\rangle$ to $|16\rangle$ for the excited states. These prove to be sufficient to explain all observed Raman modes of magnetic origin.

III. EXPERIMENTAL DETAILS

A. Sample preparation

Single crystals of Cu_2OSeO_3 were synthesized by chemical transport reaction growth. Stoichiometric amounts of CuO and SeO_2 powders (both ChemPur, 99.999%), with an addition of TeCl_4 (Sigma Aldrich, 99.999%) as transporting agent, were sealed in evacuated SiO_2 -glass ampoules. The ampoules were placed in horizontal two-zone tube furnaces, and heated to 893 K at the source side, and 773 K at the sink side of the ampoules. After a growth period of circa 40 days dark green crystals of several $\sim \text{mm}^3$ size, with well-developed $\{100\}$, $\{110\}$ and $\{111\}$ morphological faces resulted. For the Raman study a (111) oriented plate-shaped sample was prepared with a flat as-grown (111) face, and a lapped parallel opposite surface, polished with $1 \mu\text{m}$ grit size diamond paste.

B. Spontaneous Raman spectroscopy

The Raman scattering experiments were performed at low temperatures ranging from 7.5 K to 150 K. The sample is placed in a OXFORD MICROSTAT with a temperature stability of 0.1 K. The used excitation light is provided by a frequency doubled Nd:YAG (central wavelength $\lambda_C=532 \text{ nm}$) laser. The polarization for the excitation light is cleaned with a Glan Taylor polarizer. The scattered light polarization is analyzed with a sheet polarizer. We used a confocal backscattering geometry, with a $\text{NA}=0.5$ microscope objective which illuminates the sample and collects the scattered light. The excitation density was kept below 500 W/cm^2 . Laser heating effects are minimal since the 532 nm excitation falls within the transmission window of Cu_2OSeO_3 (Ref. 28) A JOBIN YVON T64000 triple subtractive spectrometer, equipped with a SYMPHONY 1024×256 charge-coupled device, was used to detect the scattered light. The resolution in the studied energy interval lies below 2 cm^{-1} . Porto notation $z(x,y)\bar{z}$ is used to indicate the polarization of the incoming (x) and scattered (y) light, with the light wave vector parallel to z. The x-polarization lies along the crystallographic $[1\bar{1}0]$ axis, and y-polarization along $[11\bar{2}]$.

IV. PHONON SCATTERING

The noncentrosymmetric cubic lattice of Cu_2OSeO_3 is described by space group $P2_13$. There are $Z=8$ chemical formula units in the structural unit cell (16 Cu^{2+} -atoms in total). This gives a total of $7 \times 8 \times 3 = 168$ phonons. There are 5 atoms on a $4a$ Wyckoff-position, and 3 atoms on a $12b$ Wyckoff-position.^{22,25}

The total Γ -point phonon spectrum is decomposed in the following irreducible representations:

$$\Gamma = 14A + 14E_1 + 14E_2 + 42T \quad (4)$$

where the acoustic phonons contribute $1T$.²⁹

The Γ -point optical phonon spectrum is decomposed in:

$$\Gamma^{\text{optical}} = 14A^{(\text{R})} + 14E_1^{(\text{R})} + 14E_2^{(\text{R})} + 41T^{(\text{R,IR})} \quad (5)$$

The threefold degenerate T-irrep phonons are Raman (R) and infrared active (IR), whereas the one-fold degenerate A, E_1 , and E_2 are only Raman-active (R). For the (111) oriented sample the A Raman modes will only show up in parallel polarization geometry, while the E_1 , E_2 , and T modes are observable in both parallel and crossed polarization geometry.²²

Figure 2 shows the phonon spectrum in $z(x,x)\bar{z}$ and $z(x,y)\bar{z}$ polarization configuration at $T=80 \text{ K}$ over the range $50\text{-}1800 \text{ cm}^{-1}$. The spectra agree with the observations of Gnezdilov *et al.* (Ref. 22), which reports the observation of 53 strong optical phonons in the frequency range up to 850 cm^{-1} and 21 weak optical phonons in the frequency range between $850\text{-}2000 \text{ cm}^{-1}$. For completeness, 26 T-phonons were detected in the infrared absorption spectrum by Miller *et al.* (Ref. 30), where also the nature of the phonons is thoroughly discussed.

Table I. The 16 isolated single cluster wave functions. The state notation is indicated by $|S, S^z\rangle_R$. The superposition for the different cluster wave functions are fully written out. $|1, 1\rangle_{A_1}$ gives the single cluster ground state. The ground state $|g_{\text{TMF}}\rangle$ in the interacting cluster model is a superposition of the states $|1, 1\rangle_{A_1}$ and $|2, 1\rangle_{A_1}$.

N	$ n\rangle$	$ S, S^z\rangle$	full wavefunction
0	1⟩	$ 1, 1\rangle_{A_1}$	$\frac{1}{2\sqrt{3}}(3 \downarrow\uparrow\uparrow\uparrow\rangle - \uparrow\downarrow\uparrow\uparrow\rangle - \uparrow\uparrow\downarrow\uparrow\rangle - \uparrow\uparrow\uparrow\downarrow\rangle)$
	2⟩	$ 1, 0\rangle_{A_1}$	$\frac{1}{\sqrt{6}}(\downarrow\downarrow\uparrow\uparrow\rangle + \downarrow\uparrow\downarrow\uparrow\rangle + \downarrow\uparrow\uparrow\downarrow\rangle - \uparrow\downarrow\downarrow\uparrow\rangle - \uparrow\downarrow\uparrow\downarrow\rangle - \uparrow\uparrow\downarrow\downarrow\rangle)$
	3⟩	$ 1, \bar{1}\rangle_{A_1}$	$\frac{1}{2\sqrt{3}}(\downarrow\downarrow\downarrow\uparrow\rangle + \downarrow\downarrow\uparrow\downarrow\rangle + \downarrow\uparrow\downarrow\downarrow\rangle - 3 \uparrow\downarrow\downarrow\downarrow\rangle)$
1	4⟩	$ 0, 0\rangle_{E_1}$	$\frac{1}{2\sqrt{3}}(2 \downarrow\downarrow\uparrow\uparrow\rangle - \downarrow\uparrow\downarrow\uparrow\rangle - \downarrow\uparrow\uparrow\downarrow\rangle - \uparrow\downarrow\downarrow\uparrow\rangle - \uparrow\downarrow\uparrow\downarrow\rangle + 2 \uparrow\uparrow\downarrow\downarrow\rangle)$
	5⟩	$ 0, 0\rangle_{E_2}$	$\frac{1}{2}(\downarrow\uparrow\downarrow\uparrow\rangle - \downarrow\uparrow\uparrow\downarrow\rangle - \uparrow\downarrow\downarrow\uparrow\rangle + \uparrow\downarrow\uparrow\downarrow\rangle)$
2	6⟩	$ 2, \bar{2}\rangle_{A_1}$	$ \downarrow\downarrow\downarrow\downarrow\rangle$
	7⟩	$ 2, \bar{1}\rangle_{A_1}$	$\frac{1}{2}(\downarrow\downarrow\downarrow\uparrow\rangle + \downarrow\downarrow\uparrow\downarrow\rangle + \downarrow\uparrow\downarrow\downarrow\rangle + \uparrow\downarrow\downarrow\downarrow\rangle)$
	8⟩	$ 2, 0\rangle_{A_1}$	$\frac{1}{\sqrt{6}}(\downarrow\downarrow\uparrow\uparrow\rangle + \downarrow\uparrow\downarrow\uparrow\rangle + \downarrow\uparrow\uparrow\downarrow\rangle + \uparrow\downarrow\downarrow\uparrow\rangle + \uparrow\downarrow\uparrow\downarrow\rangle + \uparrow\uparrow\downarrow\downarrow\rangle)$
	9⟩	$ 2, 1\rangle_{A_1}$	$\frac{1}{2}(\downarrow\uparrow\uparrow\uparrow\rangle + \uparrow\downarrow\uparrow\uparrow\rangle + \uparrow\uparrow\downarrow\uparrow\rangle + \uparrow\uparrow\uparrow\downarrow\rangle)$
	10⟩	$ 2, 2\rangle_{A_1}$	$ \uparrow\uparrow\uparrow\uparrow\rangle$
3	11⟩	$ 1, \bar{1}\rangle_{E_1}$	$\frac{1}{\sqrt{6}}(\downarrow\downarrow\downarrow\uparrow\rangle + \downarrow\downarrow\uparrow\downarrow\rangle - 2 \downarrow\uparrow\downarrow\downarrow\rangle)$
	12⟩	$ 1, \bar{1}\rangle_{E_2}$	$\frac{1}{2}(\downarrow\downarrow\downarrow\uparrow\rangle - \downarrow\downarrow\uparrow\downarrow\rangle)$
	13⟩	$ 1, 0\rangle_{E_1}$	$\frac{1}{2\sqrt{3}}(-2 \downarrow\downarrow\uparrow\uparrow\rangle + \downarrow\uparrow\downarrow\uparrow\rangle + \downarrow\uparrow\uparrow\downarrow\rangle - \uparrow\downarrow\downarrow\uparrow\rangle - \uparrow\downarrow\uparrow\downarrow\rangle + 2 \uparrow\uparrow\downarrow\downarrow\rangle)$
	14⟩	$ 1, 0\rangle_{E_2}$	$\frac{1}{2}(\downarrow\uparrow\downarrow\uparrow\rangle - \downarrow\uparrow\uparrow\downarrow\rangle + \uparrow\downarrow\downarrow\uparrow\rangle - \uparrow\downarrow\uparrow\downarrow\rangle)$
	15⟩	$ 1, 1\rangle_{E_1}$	$\frac{1}{\sqrt{6}}(-2 \uparrow\downarrow\uparrow\uparrow\rangle + \uparrow\uparrow\downarrow\uparrow\rangle + \uparrow\uparrow\uparrow\downarrow\rangle)$
	16⟩	$ 1, 1\rangle_{E_2}$	$\frac{1}{\sqrt{2}}(\uparrow\uparrow\downarrow\uparrow\rangle - \uparrow\uparrow\uparrow\downarrow\rangle)$

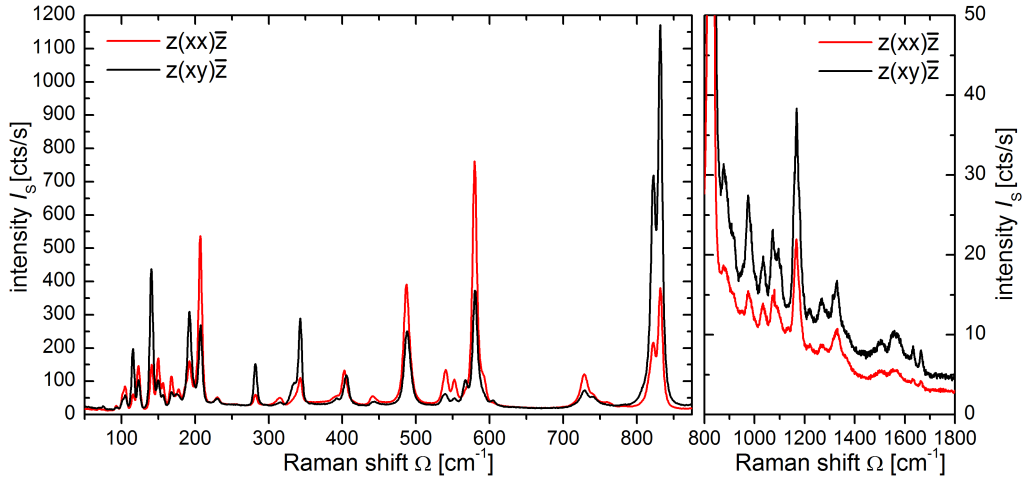


Figure 2. Phonon spectrum obtained at $T=80$ K for parallel $z(x,x)\bar{z}$ and perpendicular $z(x,y)\bar{z}$ polarization geometries. Strong phonon modes are observed in the frequency range up to 850cm^{-1} . Between 850cm^{-1} and 1800cm^{-1} weaker phonon modes are observed.

V. SPIN CLUSTER EXCITATION SCATTERING

A. Mode assignment and identification of scattering mechanism

Figure 3 shows temperature dependent Raman spectra in the range $220 - 460 \text{ cm}^{-1}$ for the $z(x,x)\bar{z}$ polarization configuration. The spectra have been normalized to the phononic scattering intensity in the region $520 - 610 \text{ cm}^{-1}$. In this energy range multiple strongly scattering modes of magnetic origin are identified: 263 cm^{-1} (M_3), 273 cm^{-1} (M_4), 300 cm^{-1} (M_5), and 425 cm^{-1} (M_6). The two weak magnetic modes at 86 cm^{-1} (M_1) and 204 cm^{-1} (M_2) are not shown.^{22,23} Two phonon modes of interest are indicated with P_1 (231 cm^{-1}) and P_2 (444 cm^{-1}).

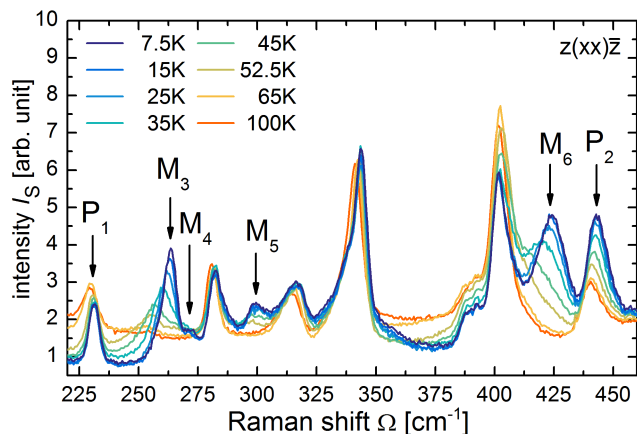


Figure 3. Normalized temperature dependent Raman spectra for Cu_2OSeO_3 in $z(x,x)\bar{z}$ polarization configuration. Four high-energy spin cluster excitations are identified within this energy range: 263 cm^{-1} (M_3), 273 cm^{-1} (M_4), 300 cm^{-1} (M_5), and 425 cm^{-1} (M_6). Two phonon modes of interest are indicated with P_1 (231 cm^{-1}) and P_2 (444 cm^{-1}).

We wish to discuss the possible cluster transitions from the ground state $|g_{\text{TMF}}\rangle$ to the excited states $|n\rangle = |2\rangle$ to $|16\rangle$ from Table I, associate the observed high-energy spin excitations with the cluster transitions, and identify the corresponding magnetic light scattering mechanism.³¹ To describe the light-matter interaction in Cu_2OSeO_3 we use the following effective Raman scattering Hamiltonian:

$$\hat{\mathcal{H}}_{\text{R}} = K \sum_{i=1:4} (\hat{S}_i^+ + \hat{S}_i^-) + \frac{1}{2}L \sum_{\substack{i,j=1:4 \\ i \neq j}} \hat{S}_i^+ \hat{S}_j^- \quad (6)$$

The four cluster spin sites are labelled by $i=1, 2, 3, 4$. The clusters are helimagnetically oriented, with the helimagnetic wave vector \mathbf{q} pointing along the $[100]$ equivalent crystallographic axes.¹³ We assume that this ordering leads to a situation where polarization selection rules are always fulfilled for a subset of the spin cluster

projections, irrespective of incident and scattered polarization geometry. Thereby, the electric field polarization selection rules are ignored,³¹ and we only discuss the linear and quadratic spin operators, as indicated in Eq. 6. The linear spin operators \hat{S}_i^\pm ($\Delta S^z = \pm 1$) correspond to Elliot-Loudon (one-magnon) scattering. Note that higher order Elliot-Loudon scattering of the form $\hat{S}_i^+ \hat{S}_i^+$ or $\hat{S}_i^- \hat{S}_i^-$ ($\Delta S^z = \pm 2$) isn't allowed in Cu_2OSeO_3 since the spin cluster consists of $S = \frac{1}{2}$ spins. The exchange scattering (two-magnon) terms are of the form $\hat{S}_i^+ \hat{S}_j^-$ and $\hat{S}_i^- \hat{S}_j^+$ ($\Delta S^z = 0$),³¹ but since these operators have the same effect on the cluster wave functions we use the notation $\frac{1}{2}\hat{S}_i^+ \hat{S}_j^-$ in Eq. 6 to avoid double counting. K and L are arbitrarily valued scattering strengths for the Elliot-Loudon and exchange scattering mechanism, respectively.

The matrix element M for the relevant spin operators $\hat{\mathcal{O}}$ of the form \hat{S}_i^+ , \hat{S}_i^- and $\hat{S}_i^+ \hat{S}_j^-$ in \mathcal{H}_{R} are determined as:

$$M = |\langle n | \hat{\mathcal{O}} | g_{\text{TMF}} \rangle|^2 \quad (7)$$

In Table II the spin cluster transitions with nonzero matrix elements and their corresponding Raman modes are indicated. Here, $|n\rangle = |S, S^z\rangle_{\text{R}}$ gives the excited cluster state, where it should be understood that $|1\rangle$ is the (isolated cluster) ground state. ΔS^z indicates the necessary change in spin projection number in order to reach the final state $|n\rangle$. When no transition is possible, this is indicated with a hyphen (-). All cluster states with a change $\Delta S^z = \pm 1, 0$ can be reached either by a one-magnon (Elliot-Loudon) or two-magnon (exchange) scattering process. All the linear and quadratic Raman spin operators which allow for a cluster transition are indicated the table. E_{A} and E_{B} give the transition energies as calculated by spin wave theory.^{16,17} The final state degeneracy is indicated in between brackets. The second-last column gives the measured Raman shifts E_{R} . M_1 to M_6 refers to the observed spin cluster excitations. The last column gives the cluster excitation energies E_{ESR} observed by electron spin resonance (ESR), as reported in Ref. 17. All energies are indicated in wavenumbers (cm^{-1}).

The 86 cm^{-1} M_1 , 204 cm^{-1} M_2 , 263 cm^{-1} M_3 , and 425 cm^{-1} M_6 modes can be unambiguously identified with different cluster transitions. All these modes are Raman-active through the Elliot-Loudon scattering mechanism (\hat{S}^\pm terms). Whether the 273 cm^{-1} M_4 Raman-mode has a $\Delta S^z = 0$ or ± 1 cannot be unambiguously identified based on the Raman data set alone. However, this mode has been observed by electron spin resonance, which shows that the mode has a $\Delta S^z = -1$ field behaviour. The Raman-activity of this mode thus also originates from the Elliot-Loudon mechanism. The 300 cm^{-1} M_5 Raman-mode may either be a transition to $|2, 0\rangle_{\text{A}_1}$ by a \hat{S}^- scattering process, or $|2, 1\rangle_{\text{A}_1}$ by a $\hat{S}^+ \hat{S}^-$ scattering process. This mode was not observed in the

ESR study (indicated with an X). The scattering mechanism of the 300 cm^{-1} M_5 mode can thus not be unambiguously defined given the present data set and previous works. Scattering to the $|15\rangle$ or $|16\rangle$ excited state (expected excitation energy $\approx 400\text{ cm}^{-1}$) is Raman-allowed. This mode however could not be unambiguously resolved due to the presence of a strong phonon mode. For completeness we've indicated the 0 cm^{-1} M_G in the table, which is the magnetic Goldstone mode of Cu_2OSeO_3 . The M_G -mode was observed in the electron spin resonance study. All discussed modes are indicated in Table II.

B. Temperature dependence of spin cluster excitations

For the spin cluster excitations a spectral weight transfer to lower Raman shift Ω is observed when the temperature increases towards T_C (see Fig. 3). The magnetic spectral weight transfer is understood as a softening and broadening of the high-energy spin excitations. In Fig. 4a-c we show the scattering region around the M_3 spin cluster mode and the P_1 phonon in closer detail for temperatures below and above T_C . The scattering region is fitted with a sum of Lorentzian fit functions. The red line shows the full fit and the blue and green lines the fits for the P_1 phonon and M_3 spin excitation, respectively. Above T_C the M_3 excitation has significantly broadened and a weak phonon becomes visible (P^*). The broadening above T_C has previously been identified in the terahertz transmission of Cu_2OSeO_3 .²⁰

The frequency $\Omega(T)$ of the M_3 excitation is plotted in Fig. 4d. Below T_C the temperature dependence of the excitation energy can be well-described by a scaling law of the form $\Omega(T) \propto (T_C - T)/T_C^\gamma$, with $\gamma \approx 0.02$ as exponent. Above $T_C \approx 58\text{ K}$ magnetic scattering still persists, but the spin excitations have significantly broadened into a continuum type of magnetic scattering.²³ This is most clearly seen in Fig. 4c for M_3 ($\Delta S^z = +1$). For M_4 ($\Delta S^z = -1$) similar qualitative behaviour is observed, as most clearly seen in Fig. 3. Above T_C the fitting of the M_3 peak position becomes unreliable. The temperature dependent spectral weight of M_3 is plotted in Fig. 4f. Up till T_C the spectral weight remains constant. Above T_C the determination of the spectral weight becomes unreliable.

Figure 4e shows the temperature dependence of the line width at half maximum (inverse decay rate) of the M_3 excitation. The functional temperature dependence below T_C is well fitted by the second order polynomial $\frac{\Gamma}{2}(T) = \frac{\Gamma_0}{2}(T=0) + A \cdot T + B \cdot T^2$, with the largest contributions formed by $\frac{\Gamma_0}{2}(T=0)$ and $B \cdot T^2$. The latter process describes a four magnon interaction.²⁰ The large finite $\frac{\Gamma_0}{2}(T=0)$ term may result from inhomogeneous broadening from disorder. However, Laurita *et al.* (Ref. 20) argue that the spontaneous decay rate of spin cluster excitations in Cu_2OSeO_3 instead may originate from

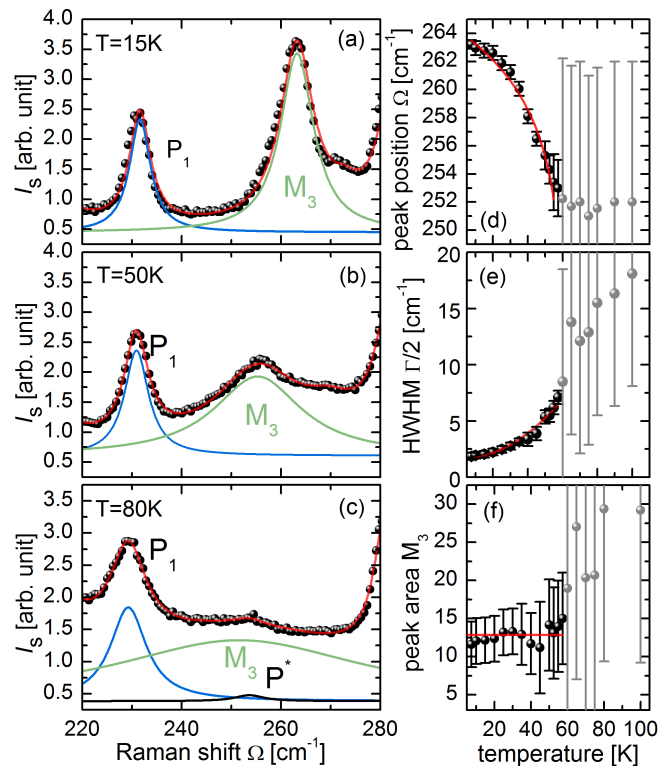


Figure 4. (a-c) Scattering region around the M_3 spin cluster mode and the P_1 phonon for temperatures below and above T_C . (d) Temperature dependence of the M_3 spin excitation energy. Below T_C the temperature dependent position is well-fitted with a scaling function of the form $\Omega(T) \propto (T_C - T)/T_C^\gamma$, with $\gamma \approx 0.02$ as exponent (red curve). (e) Temperature dependent spectral weight of the M_3 spin excitation. Below $T_C \approx 58\text{ K}$ the spectral weight remains constant (red curve). Above $T_C \approx 58\text{ K}$ the determination of the spectral weight becomes unreliable, however, it stays finite. (f) Half width at half maximum (inverse decay rate) of the M_1 spin excitation. Below T_C a quadratic power law is observed, in addition to a strong spontaneous decay rate.

quantum fluctuations.

The temperature dependence of the magnetic scattering across the phase transition of the high-energy spin excitations in Cu_2OSeO_3 is rather peculiar in light of the vast range of historic and contemporary magnetic Raman scattering literature.^{32,33} In the case of single spin (anti-)ferromagnets, such as NiF_2 or KNiF_3 , the first order (Elliott-Loudon) scattering originates from low-energy zone-*center* magnons. The Γ -point one-magnon scattering vanishes above the (anti-)ferromagnetic critical temperature $T_{N/C}$, where the long-range spin correlation is strongly reduced. Exchange scattering from high-energy zone-*edge* magnon pairs, described by the pair-operators $\hat{S}^+ S^-$ and $\hat{S}^- \hat{S}^+$ ($\Delta S^z = 0$), is possible in antiferromagnets above T_N , since short-range correlations still exist.^{31,32}

The formation of Cu_4 spin clusters far above the long-range ordering temperature $T_C \approx 58\text{ K}$,¹⁹ and the result-

Table II. Magnetic Raman modes, spin cluster excitation energies, and Raman operators. $|n\rangle$ and $|S, S^z\rangle_R$ indicate the final state. The full wavefunctions were given in Table I. The column ΔS^z gives the change in total cluster spin projection number. Raman operators which allow a specific scattering process between the ground state $|g_{\text{TMMF}}\rangle$, and excited states $|2\rangle$ to $|16\rangle$, are indicated in the columns 1-magnon and 2-magnon. One-magnon scattering is only possible via the Elliot-Loudon mechanism (\hat{S}^\pm terms). In the case of Cu_2OSeO_3 , only the exchange scattering type of 2-magnon scattering is possible, as indicated by Raman operators of a $\hat{S}^+\hat{S}^-$ form. When no transition between the cluster ground state and excited state is allowed by the respective Raman operator, this is indicated with a hyphen (-). E_A and E_B give the spin wave theory calculated transition energies, as obtained in the work of Refs. 17 and 16. The degeneracy of the final state is indicated in between brackets. The second-last column gives the measured Raman shifts E_R . The last column gives the cluster excitation energies E_{ESR} observed by electron spin resonance (ESR), as reported in Ref. 17. All energies are indicated in wavenumbers (cm^{-1}). The Raman-modes at 263 cm^{-1} (M_3) and 425 cm^{-1} (M_6) can be unambiguously identified with an \hat{S}^- and \hat{S}^+ transition, which are Raman-active through the Elliot-Loudon scattering mechanism. The weak modes 86 cm^{-1} (M_1) and 204 cm^{-1} (M_4) can be also identified with \hat{S}^- and \hat{S}^+ transitions, respectively. Combined with the ESR result, the 273 cm^{-1} M_4 Raman-mode can be identified as a transition to $|0, 0\rangle_E$ via a \hat{S}^- operator. The 300 cm^{-1} M_5 Raman-mode may either be a transition to $|2, 0\rangle_{A_1}$ via \hat{S}^- , or $|2, 1\rangle_{A_1}$ via $\hat{S}^+\hat{S}^-$ terms. This mode was not observed in the ERS study (indicated with an X). The Raman-mode corresponding to a transition to $|1, 1\rangle_E$ (expected excitation energy $\approx 400\text{ cm}^{-1}$) could not be unambiguously identified (indicated with an X). The 0 cm^{-1} M_G mode corresponds to the magnetic Goldstone mode, and was observed in the ESR-study (Ref. 17).

$ n\rangle$	final state $ S, S^z\rangle$	ΔS^z	1-magnon (Elliot-Loudon)	2-magnon (exchange scattering)	$E_1[\text{cm}^{-1}]$	$E_2[\text{cm}^{-1}]$	$E_R[\text{cm}^{-1}]$	$E_{\text{ESR}}[\text{cm}^{-1}]$
$ 1\rangle$	$ 1, 1\rangle_{A_1}$	0	-	-	-	-	-	-
$ 2\rangle$	$ 1, 0\rangle_{A_1}$	-1	$\hat{S}_1^-, \hat{S}_2^-, \hat{S}_3^-, \hat{S}_4^-$	-	$0(1)$	$96(3)$	$85(M_1)$	$0(M_G)$ $85(M_1)$
$ 3\rangle$	$ 1, \bar{1}\rangle_{A_1}$	-2	-	-	$159(4)$	-	-	-
$ 4\rangle$	$ 0, 0\rangle_{E_1}$	-1	$\hat{S}_2^-, \hat{S}_3^-, \hat{S}_4^-$	-	$236(3)$	$276(5)$	$273(M_4)$	$270(M_4)$
$ 5\rangle$	$ 0, 0\rangle_{E_2}$	-1	\hat{S}_3^-, \hat{S}_4^-	-				
$ 6\rangle$	$ 2, \bar{2}\rangle_{A_1}$	-3	-	-	$338(4)$	-	-	-
$ 7\rangle$	$ 2, \bar{1}\rangle_{A_1}$	-2	-	-	$335(4)$	-	-	-
$ 8\rangle$	$ 2, 0\rangle_{A_1}$	-1	$\hat{S}_1^-, \hat{S}_2^-, \hat{S}_3^-, \hat{S}_4^-$	-	$310(1)$	$314(3)$	$300(M_5?)$	X
$ 9\rangle$	$ 2, 1\rangle_{A_1}$	0	-	$\hat{S}_1^+ \hat{S}_2^-, \hat{S}_1^+ \hat{S}_3^-, \hat{S}_1^+ \hat{S}_4^-, \hat{S}_2^+ \hat{S}_1^-,$ $\hat{S}_2^+ \hat{S}_3^-, \hat{S}_2^+ \hat{S}_4^-, \hat{S}_3^+ \hat{S}_1^-, \hat{S}_3^+ \hat{S}_2^-,$ $\hat{S}_3^+ \hat{S}_4^-, \hat{S}_4^+ \hat{S}_1^-, \hat{S}_4^+ \hat{S}_2^-, \hat{S}_4^+ \hat{S}_3^-$	$272(1)$	$288(3)$	$300(M_5?)$	-
$ 10\rangle$	$ 2, 2\rangle_{A_1}$	+1	$\hat{S}_1^+, \hat{S}_2^+, \hat{S}_3^+, \hat{S}_4^+$	-	$206(1)$	$260(3)$	$204(M_2)$ $263(M_3)$	$202(M_2)$ $263(M_3)$
$ 11\rangle$	$ 1, \bar{1}\rangle_{E_1}$	-2	-	-	$380(8)$	-	-	-
$ 12\rangle$	$ 1, \bar{1}\rangle_{E_2}$	-2	-	-				
$ 13\rangle$	$ 1, 0\rangle_{E_1}$	-1	$\hat{S}_2^-, \hat{S}_3^-, \hat{S}_4^-$	-	$419(8)$	-	$425(M_6)$	$420(M_6)$
$ 14\rangle$	$ 1, 0\rangle_{E_2}$	-1	\hat{S}_3^-, \hat{S}_4^-	-				
$ 15\rangle$	$ 1, 1\rangle_{E_1}$	0	-	$\hat{S}_1^+ \hat{S}_2^-, \hat{S}_1^+ \hat{S}_3^-, \hat{S}_1^+ \hat{S}_4^-,$ $\hat{S}_2^+ \hat{S}_3^-, \hat{S}_2^+ \hat{S}_4^-, \hat{S}_3^+ \hat{S}_1^-,$ $\hat{S}_3^+ \hat{S}_4^-, \hat{S}_4^+ \hat{S}_2^-, \hat{S}_4^+ \hat{S}_3^-$	$396(3)$	$401(5)$	X	-
$ 16\rangle$	$ 1, 1\rangle_{E_2}$	0	-	$\hat{S}_1^+ \hat{S}_3^-, \hat{S}_1^+ \hat{S}_4^-, \hat{S}_2^+ \hat{S}_3^-,$ $\hat{S}_2^+ \hat{S}_4^-, \hat{S}_3^+ \hat{S}_4^-, \hat{S}_4^+ \hat{S}_3^-$				

ing high-energy dispersive magnon branch below T_C results in the possibility to scatter from zone-center *internal spin cluster* excitations above and below T_C by the Elliot-Loudon mechanism.^{31,32} Below T_C high-energy *optical magnon* branches are well-defined and dispersive by the inter-cluster correlation. A cartoon is provided in Fig. 5a. Raman-scattering by the Elliot-Loudon mechanism is possible at the Γ -point (indicated with orange squares). However, above T_C inter-cluster correlations are lost. Here the high-energy spin cluster excitations are thus of fully cluster-internal nature.³⁴ The broad magnetic scattering evidences that the uncoupled clusters reside in an inhomogeneous environment and/or that the lifetime of the cluster-internal spin cluster excitations is short. In reciprocal space this corresponds to a broad dispersionless band of localized cluster-internal spin excitations,³⁴ as depicted in Fig. 5b. This finite localized spin cluster excitation density-of-states at the Γ -point above T_C still allows for first-order scattering, but however will appear as broad continuum of magnetic scattering, as indicated with the orange rectangle.³⁴ We stress out that it is thus the spin cluster nature with resulting Γ -point optical magnons, which make the one-magnon excitations of high enough energy to be observable in Cu_2OSeO_3 . This is in sharp contrast to simple antiferromagnets, where a relatively strong magnetocrystalline anisotropy is necessary to observe one-magnon excitations by Raman spectroscopy.

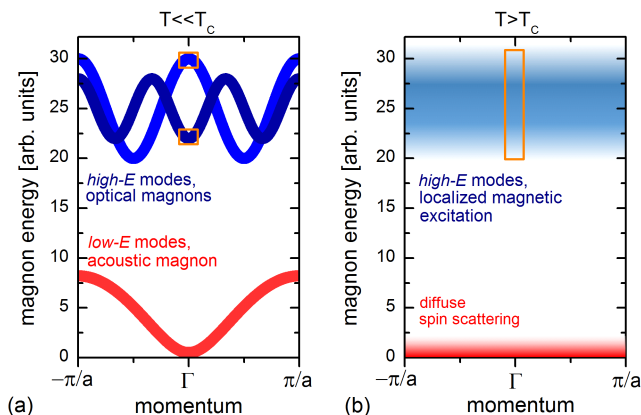


Figure 5. Cartoon picture of the spin excitation dispersion of a cluster magnet below and above the critical temperature T_C . (a) A cluster magnet has well-defined low-energy *external* spin cluster excitation branches (red) and high energy *internal* spin cluster excitation branches (blue) below T_C . Raman-scattering from high-energy spin cluster excitations is possible at the Γ -point, as indicated with orange squares. (b) Above T_C the high-energy internal spin cluster excitation branches cross over into a broad dispersionless band of localized magnetic excitations (blue). The low energy external branch vanishes above T_C due to the loss of inter-cluster correlations, leading to diffuse spin scattering. Raman-scattering from localized high-energy spin cluster excitations is possible at the Γ -point, as indicated with the orange rectangle.

C. Magnetoelastic coupling

Cu_2OSeO_3 is a rare example of a magnetoelectric material with *pd*-hybridization as coupling mechanism.¹² The magnetoelectric coupling for instance allows to control the angular orientation of the skyrmion lattice.^{35,36} Different reports addressed that no significant magnetostrictive lattice contraction nor a structural symmetry change occurs in the magnetically ordered phase,^{23,25} even though the natural optical activity shows an enhancement in the helimagnetic phase.²⁸ This is in line with that Cu_2OSeO_3 has *pd*-hybridization as the dominant magnetoelectric coupling mechanism. However, this observation does not imply that magnetoelastic coupling is completely absent in Cu_2OSeO_3 . Evidences of a finite magnetoelastic coupling are, for instance, the anomalies in optical phonon frequencies around T_C ^{22,23,30} and the observation that the propagation of acoustic phonons is nonreciprocal in Cu_2OSeO_3 .³⁷

In Fig. 6a we plot the phonon energy and half width at half maximum (HWHM) for the phonon P_1 . Figure 6a shows the phonon energy and spectral weight (SW) for the phonon P_2 . All plotted phonon parameters show strong sensitivity to magnetic ordering. This is especially the case for the P_2 phonon, as for instance seen from the spectral weight, but also directly in Fig. 3. Neither, the spin wave theory calculations, nor neutron experiments evidence the presence of a spin cluster excitation around 444 cm^{-1} . Instead, the P_2 mode corresponds to the vibration of the CuO_5 pyramidal units.³⁰ The similar energy scale and overlapping dispersion of optical phonons and high-energy spin cluster excitations can lead to a phonon-magnon hybridization by magnetoelastic coupling.³⁷⁻³⁹ This in turn will lead to a strong temperature dependence for the line-width, position and spectral weight of the optical phonons.

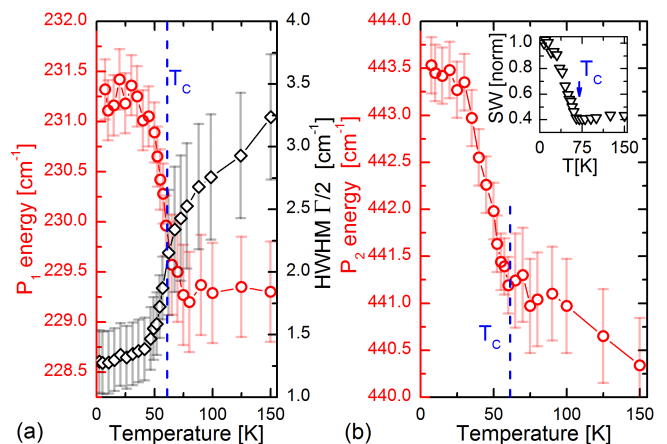


Figure 6. (a) P_1 phonon energy and half width at full maximum (HWHM) and (b) P_2 phonon energy with the normalized spectral weight SW as inset. Around the magnetic critical temperature $T_C \approx 58\text{ K}$ an anomaly is observed in the P_1 and P_2 phonon parameters.

VI. CONCLUSIONS

A Raman spectroscopy study of the cluster Mott insulator Cu_2OSeO_3 was performed. Multiple high-energy spin cluster excitations were observed besides a rich phonon spectrum. We systematically characterized the observed spin cluster transitions along the lines of the Cu_2OSeO_3 spin cluster model and deduced that the Raman activity of the spin cluster excitations originates in the first order Elliot-Loudon light scattering mechanism. The high energy spin cluster excitation modes show to soften and broaden with increasing temperature and persist above T_C as a broad magnetic scattering continuum. Above T_C , the Cu_4 clusters are decoupled, resulting in localized cluster-internal spin excitations. In the long-range ordered phase the internal cluster modes acquire dispersion by the inter-cluster exchange interactions, and form optical magnon branches, resulting in well-defined magnetic modes in the Raman spectrum. Our observa-

tions support the picture that Cu_2OSeO_3 can be regarded as a solid-state molecular crystal of spin nature.

ACKNOWLEDGMENTS

This project was partially financed by the Deutsche Forschungsgemeinschaft (DFG) through Project No. 277146847 - Collaborative Research Center 1238: Control and Dynamics of Quantum Materials (Subprojects No. A02 and No. B03). RBV acknowledges funding through the Bonn-Cologne Graduate School of Physics and Astronomy (BCGS). All authors thank D. I. Khomskii (Cologne, DE) and L. Bohatý (Cologne, DE) for fruitful discussions. RBV thanks D. Inosov (Dresden, DE), I. Rousochatzakis (Loughborough University, UK) and J. Romhányi (Okinawa, JP) for fruitful discussions on their Cu_2OSeO_3 spin cluster publications.

* Corresponding author: versteeg@ph2.uni-koeln.de

† Corresponding author: pvl@ph2.uni-koeln.de

- ¹ P. Fazekas, *Lecture notes on electron correlation and magnetism* (World scientific, 1999).
- ² D. I. Khomskii, *Transition metal compounds* (Cambridge University Press, 2014).
- ³ J. P. Attfield, Orbital molecules in electronic materials. *APL Mater.* **3**, 17 (2015).
- ⁴ S. V. Streltsov and D. I. Khomskii, Orbital physics in transition metal compounds: new trends, *Phys. Usp.* **60**, 1121 (2017).
- ⁵ M. S. Senn, J. P. Wright, and J. P. Attfield, Charge order and three-site distortions in the Verwey structure of magnetite, *Nature* **481**, 173 (2012).
- ⁶ S. de Jong, R. Kukreja, C. Trabant, N. Pontius, C. F. Chang, T. Kachel, M. Beye, F. Sorgenfrei, C. H. Back, B. Bräuer, W. F. Schlotter, J. J. Turner, O. Krupin, M. Doehler, D. Zhu, M. A. Hossain, A. O. Scherz, D. Fausti, F. Novelli, M. Esposito, W. S. Lee, Y.-D. Chuang, D. H. Lu, R. G. Moore, M. Yi, M. Trigo, P. Kirchmann, L. Pathy, M. S. Golden, M. Buchholz, P. Metcalf, F. Parmigiani, W. Wurth, A. Föhlisch, C. Schüßler-Langeheine, and H. A. Dürr, Speed limit of the insulator-metal transition in magnetite, *Nat. Mater.* **12**, 882 (2013).
- ⁷ A. Revelli, M. Moretti Sala, G. Monaco, P. Becker, L. Bohatý, M. Hermanns, T. C. Koethe, T. Fröhlich, P. Warzanowski, T. Lorenz, S. V. Streltsov, P. H. M. van Loosdrecht, D. I. Khomskii, J. van den Brink and M. Grüninger, Resonant inelastic x-ray incarnation of Young's double-slit experiment, *Sci. Adv.* **5**, eaav4020 (2019).
- ⁸ S. A. J. Kimber, I. I. Mazin, J. Shen, H. O. Jeschke, S. V. Streltsov, D. N. Argyriou, R. Valentí, and D. I. Khomskii, Valence bond liquid phase in the honeycomb lattice material Li_2RuO_3 , *Phys. Rev. B* **89**, 081408 (2014).

- ⁹ P. W. Anderson, The resonating valence bond state in La_2CuO_4 and superconductivity, *Science* **235**, 1196 (1987).
- ¹⁰ G. Venkataraman and V. C. Sanhi, External vibrations in complex crystals. *Rev. Mod. Phys.* **42**, 409 (1970).
- ¹¹ I. Natkaniec, E. L. Bokhenkov, B. Dorner, J. Kalus, G. A. Mackenzie, G. S. Pawley, U. Schmelzer, and E. F. Sheka, Phonon dispersion in d_8 -naphthalene crystal at 6K, *J. Phys. C: Solid State Physics* **13**, 4265 (1989).
- ¹² S. Seki, X. Z. Yu, S. Ishiwata, and Y. Tokura, Observation of skyrmions in a multiferroic material, *Science* **336**, 198 (2012).
- ¹³ T. Adams, A. Chacon, M. Wagner, A. Bauer, G. Brandl, B. Pedersen, H. Berger, P. Lemmens, and C. Pfleiderer, Long-wavelength helimagnetic order and skyrmion lattice phase in Cu_2OSeO_3 , *Phys. Rev. Lett.* **108**, 237204 (2012).
- ¹⁴ S. Seki, J.-H. Kim, D. S. Inosov, R. Georgii, B. Keimer, S. Ishiwata, and Y. Tokura, Formation and rotation of skyrmion crystal in the chiral-lattice insulator Cu_2OSeO_3 , *Phys. Rev. B* **85**, 220406 (2012).
- ¹⁵ O. Janson, I. Rousochatzakis, A. A. Tsirlin, M. Belesi, A. A. Leonov, U. K. Rößler, J. Van den Brink, and H. Rosner, The quantum nature of skyrmions and half-skyrmions in Cu_2OSeO_3 , *Nat. Commun.* **5**, 5376 (2014).
- ¹⁶ J. Romhányi, J. van den Brink, and I. Rousochatzakis, Entangled tetrahedron ground state and excitations of the magnetoelectric skyrmion material Cu_2OSeO_3 , *Phys. Rev. B* **90**, 140404 (2014).
- ¹⁷ M. Ozerov, J. Romhányi, M. Belesi, H. Berger, J.-Ph. Ansermet, Jeroen van den Brink, J. Wosnitza, S. A. Zvyagin, and I. Rousochatzakis, Establishing the fundamental magnetic interactions in the chiral skyrmionic Mott insulator Cu_2OSeO_3 by terahertz electron spin resonance, *Phys. Rev. Lett.* **113**, 157205 (2014).
- ¹⁸ P. Y. Portnichenko, J. Romhányi, Y. A. Onykienko, A. Henschel, M. Schmidt, A. S. Cameron, M. A. Surmach, J. A. Lim, J. T. Park, A. Schneidewind, D. L. Abernathy, H. Rosner, J. van den Brink, and D. Inosov, Magnon spectrum of the helimagnetic insulator Cu_2OSeO_3 , *Nat. Com-*

- mun. **7**, 10725 (2016).
- ¹⁹ G. S. Tucker, J. S. White, J. Romhányi, D. Szaller, I. Kézsmárki, B. Roessli, U. Stuhr, A. Magrez, F. Groitl, P. Babkevich, P. Huang, I. Živković, and H. M. Rønnow. Spin excitations in the skyrmion host Cu_2OSeO_3 , *Phys. Rev. B* **93**, 054401 (2016).
 - ²⁰ N. J. Laurita, G. G. Marcus, B. A. Trump, J. Kindervater, M. B. Stone, T. M. McQueen, C. L. Broholm, and N. P. Armitage, Low-energy magnon dynamics and magneto-optics of the skyrmionic Mott insulator Cu_2OSeO_3 , *Phys. Rev. B* **95**, 235155 (2017).
 - ²¹ R. B. Versteeg, J. Zhu, C. Boguschewski, F. Sekiguchi, A. Sahasrabudhe, K. Budzinauskas, P. Padmanabhan, P. Becker, D. I. Khomskii, and P. H. M. van Loosdrecht, Coupled dynamics of long-range and cluster-internal spin order in the cluster Mott insulator Cu_2OSeO_3 , *Phys. Rev. B* **100**, 064401 (2019).
 - ²² V. P. Gnezdilov, K. V. Lamonova, Y. G. Pashkevich, P. Lemmens, H. Berger, F. Bussy, and S. L. Gnatchenko, Magnetoelectricity in the ferrimagnetic Cu_2OSeO_3 : symmetry analysis and Raman scattering study, *Low Temp. Phys.* **36**, 550 (2010).
 - ²³ V. S. Kurnosov, V. P. Gnezdilov, V. V. Tsapenko, P. Lemmens, and H. Berger, Analysis of the low-frequency spectrum of the cubic noncentrosymmetric ferrimagnet Cu_2OSeO_3 , *Low Temp. Phys.* **38**, 489 (2012).
 - ²⁴ See Fig. 3 in Ref. 19 for the hexagonal exchange path.
 - ²⁵ J.-W. G. Bos, C. V. Colin, and T. T. M. Palstra, Magnetoelectric coupling in the cubic ferrimagnet Cu_2OSeO_3 , *Phys. Rev. B* **78**, 094416 (2008).
 - ²⁶ J. H. Yang, Z. L. Li, X. Z. Lu, M.-H. Whangbo, S.-H. Wei, X. G. Gong, and H. J. Xiang, Strong Dzyaloshinskii-Moriya interaction and origin of ferroelectricity in Cu_2OSeO_3 , *Phys. Rev. Lett.* **109**, 107203 (2012).
 - ²⁷ E. J. Samuelsen and M. Melamud, Antiferromagnetism with alternating strong and weak coupling, *J. Phys. C: Solid State Physics* **6**, 3305 (1973).
 - ²⁸ R. B. Versteeg, I. Vergara, S. D. Schäfer, D. Bischoff, A. Aqeel, T. T. M. Palstra, M. Grüniger, and P. H. M. van Loosdrecht, Optically probed symmetry breaking in the chiral magnet Cu_2OSeO_3 , *Phys. Rev. B* **94**, 094409 (2016).
 - ²⁹ M. I. Aroyo, A. Kirov, C. Capillas, J. M. Perez-Mato, and H. Wondratschek, *Bilbao Crystallographic Server. II. Representations of crystallographic point groups and space groups*, *Acta Crystallogr. Sect. A* **62**, 115 (2006).
 - ³⁰ K. H. Miller, X. S. Xu, H. Berger, E. S. Knowles, D. J. Arenas, M. W. Meisel, and D. B. Tanner, Magnetodielectric coupling of infrared phonons in single-crystal Cu_2OSeO_3 , *Phys. Rev. B* **82**, 144107 (2010).
 - ³¹ P. A. Fleury and R. Loudon, Scattering of light by one- and two-magnon excitations, *Phys. Rev.* **166**, 514 (1968).
 - ³² M. G. Cottam and D. J. Lockwood, *Light scattering in magnetic solids*, (Wiley New York, NY, 1986).
 - ³³ T. P. Devereaux and R. Hackl, Inelastic light scattering from correlated electrons, *Rev. Mod. Phys.* **79**, 175 (2007).
 - ³⁴ S. H. Liu, Magnetic excitations above the critical temperature, *Phys. Rev. B* **13**, 2979 (1976).
 - ³⁵ J.S. White, K. Prša, P. Huang, A. A. Omrani, I. Živković, M. Bartkowiak, H. Berger, A. Magrez, J. L. Gavilano, G. Nagy, J. Zang, and H. M. Rønnow, Electric-field-induced skyrmion distortion and giant lattice rotation in the magnetoelectric insulator Cu_2OSeO_3 , *Phys. Rev. Lett.* **113**, 107203 (2014).
 - ³⁶ J. S. White, I. Živković, A. J. Kruchkov, M. Bartkowiak, A. Magrez, and H. M. Rønnow, Electric-field-driven topological phase switching and Skyrmion-lattice metastability in magnetoelectric Cu_2OSeO_3 , *Phys. Rev. Applied* **10**, 014021 (2018).
 - ³⁷ T. Nomura, X.-X. Zhang, S. Zherlitsyn, J. Wosnitza, Y. Tokura, N. Nagaosa, and S. Seki, Phonon magnetochiral effect, *Phys. Rev. Lett.* **122**, 145901 (2019).
 - ³⁸ C. Kittel, Interaction of spin waves and ultrasonic waves in ferromagnetic crystals, *Phys. Rev.* **110**, 836 (1958).
 - ³⁹ Y. R. Shen and N. Bloembergen, Interaction between light waves and spin waves, *Phys. Rev.* **143**, 372 (1966).